# POTENTIAL MATCHING OPTIMAL TRANSPORT: CONTINUOUS NORMALIZING FLOWS FOR EXACT $p$-WASSERSTEIN DYNAMICS

**Anonymous authors**
Paper under double-blind review

## ABSTRACT

We introduce Potential Matching Optimal Transport (PMOT), a potential-flow framework for general $p$-cost optimal transport with $c_p(x, y) = \|x - y\|^p$. PMOT parameterizes the CNF velocity field with a scalar potential in the generalized Benamou–Brenier form for the chosen exponent $p$. It trains the potential gradient with a self-induced matching loss along straight bridges determined by the model's own endpoints, while allowing flexible terminal distribution matching. Our main result establishes zero-loss exactness: under the stated regularity, exact terminal matching, and uniqueness assumptions, any zero-loss solution satisfies the generalized Benamou–Brenier optimality system and recovers the corresponding $p$-optimal transport map and dynamics. On synthetic benchmarks, PMOT learns $p$-specific maps that agree with the corresponding $p$-matched OT references. On three high-dimensional tabular datasets, it attains lower NLL than the evaluated OT-Flow configurations, and an MMD-based color transformation experiment illustrates flexible sample-based terminal matching.

## 1 INTRODUCTION

Continuous Normalizing Flows (CNFs) learn invertible transformations between data distributions and tractable reference priors through time-dependent ODE dynamics (Chen et al., 2018; Grathwohl et al., 2018). They support exact likelihood evaluation via the continuous change-of-variables formula while simultaneously defining a transport trajectory between distributions. This makes CNFs a natural interface between likelihood-based generative modeling and optimal transport (OT).

A particularly influential line of work connects CNFs with OT by regularizing the learned dynamics toward low-cost transport paths. OT-Flow (Onken et al., 2021), for example, introduces a potential-flow parameterization together with a kinetic-energy regularizer, yielding a likelihood-based model whose dynamics are closely related to the Benamou–Brenier formulation of quadratic-cost optimal transport (Benamou & Brenier, 2000). However, the resulting geometry is naturally tied to the quadratic cost, or equivalently the $W_2$ geometry. Many OT problems are instead defined by more general costs

$$c_p(x, y) = \|x - y\|^p,$$

where the exponent $p$ controls the induced transport geometry and, especially in asymmetric transport problems, can lead to different optimal couplings and trajectories (Villani, 2009; Peyré & Cuturi, 2019). This motivates likelihood-based potential flows whose dynamics are aligned not only with the quadratic case, but also with general $p$-cost OT.

In this work, we introduce *Potential Matching Optimal Transport* (PMOT), a potential-flow framework for general $p$-cost optimal transport with terminal distribution matching. PMOT preserves the main structural advantages of OT-Flow-style CNFs when instantiated with a KL/NLL terminal loss: the dynamics remain continuous, and likelihoods are evaluated through the CNF change-of-variables formula. PMOT parameterizes the velocity field in the generalized Benamou–Brenier form with conjugate exponent $q = p/(p - 1)$, thereby making the dynamics depend on the target $p$-cost geometry. Rather than using a quadratic kinetic-energy penalty, PMOT introduces a self-induced potential matching residual. For each data sample $x$, the current CNF produces a terminal endpoint



Reviewers: please read the Reviewer Guidelines (iclr.cc/Conferences/2027/ReviewerGuidelines) and the AI Policy for Reviewers (iclr.cc/Conferences/2027/AIPolicyForReviewers). If you used AI to expand, edit, or polish your review, please provide the input text to the LLM. Better still, consider skipping the LLM and submitting your original text: we, and the authors, are much more interested in your unedited thoughts than in what an LLM has to say. AI-assisted or not, you are putting your name and reputation behind your review: LLM-generated falsehoods, hallucinations or misrepresentations are subject to disciplinary action, which may include desk-rejecting all papers you have authored.

$F_\theta(x)$, and the residual matches the potential gradient along the induced straight bridge to

$$-\|F_\theta(x) - x\|^{p-2}\big(F_\theta(x) - x\big).$$

This condition is equivalent to matching the induced velocity to the constant-speed bridge velocity. It requires no precomputed OT coupling and instead imposes consistency on the model's own endpoint map.

The central theoretical property of PMOT is a zero-loss exactness result. Under the stated regularity, exact terminal matching, and uniqueness assumptions, every zero-loss solution satisfies the generalized Benamou–Brenier optimality system for the corresponding $p$-cost problem. Consequently, in this idealized limit, the induced flow recovers the exact $p$-Wasserstein dynamics and attains the optimal transport cost. In finite-sample neural training, this exactness is subject to empirical sampling, model capacity, numerical integration, and optimization error; our empirical claims are therefore stated in terms of alignment with $p$-matched OT references rather than unconditional exact recovery. Accordingly, we evaluate geometric fidelity using post-hoc OT references computed with the same exponent as the trained model.

We evaluate PMOT on synthetic transport, high-dimensional tabular density estimation, and image color transformation. The experiments assess $p$-matched geometric alignment, generation under mild objective weighting, likelihood-based density modeling, and MMD-based sample transport.

Our contributions are summarized as follows:

- We introduce PMOT, a potential-flow CNF framework for general $p$-cost optimal transport, trained through self-induced potential matching without external OT couplings or inner OT optimization.
- We prove that, under the theorem's assumption, every zero-loss PMOT solution recovers the corresponding $p$-optimal transport map and dynamics.
- We evaluate each model against OT references computed with the matching cost exponent and demonstrate $p$-specific geometric alignment, competitive likelihood modeling, and flexible terminal matching through KL/NLL and MMD objectives.

## 2 Preliminaries

### 2.1 General $p$-Cost OT and Displacement Interpolation

Let $\mu_0, \mu_1$ be probability measures on $\mathbb{R}^d$ with finite $p$-th moments. For $p \geq 1$, the $p$-cost optimal transport problem is

$$W_p^p(\mu_0, \mu_1) = \inf_{\pi \in \Pi(\mu_0, \mu_1)} \int \|x - y\|^p \, \mathrm{d}\pi(x, y).$$

When an optimal Monge map $T_p$ exists, it satisfies $T_{p\#}\mu_0 = \mu_1$ and attains the same cost. Its displacement interpolation is

$$X_t(x) = (1-t)x + tT_p(x), \qquad \rho_t = (X_t)_\#\mu_0,$$

with velocity

$$u_p(t, X_t(x)) = T_p(x) - x.$$

This path attains the dynamic $p$-cost:

$$\int_0^1 \int_{\mathbb{R}^d} \|u_p(t,z)\|^p \, \mathrm{d}\rho_t(z) \, \mathrm{d}t = \int_{\mathbb{R}^d} \|T_p(x) - x\|^p \, \mathrm{d}\mu_0(x) = W_p^p(\mu_0, \mu_1).$$

### 2.2 Benamou–Brenier Optimality and Potential Velocities

The same $p$-cost transport problem has a dynamic Benamou–Brenier formulation(Santambrogio, 2015). The dynamic problem is

$$\inf_{\rho, v} \frac{1}{p} \int_0^1 \int_{\mathbb{R}^d} \|v(t,x)\|^p \, d\rho_t(x) \, dt$$

subject to the endpoint constraints $\rho_{t=0} = \mu_0$, $\rho_{t=1} = \mu_1$ and the continuity equation

$$\partial_t \rho_t + \nabla_x \cdot (\rho_t v) = 0.$$

In a smooth formal derivation, the scalar field $\Phi(t, x)$ appears as the Lagrange multiplier for this continuity-equation constraint. The corresponding Euler–Lagrange condition with respect to the velocity gives on the support of $\rho_t$ that

$$\|v\|^{p-2} v = -\nabla_x \Phi.$$

Since $p > 1$, the map $z \mapsto \|z\|^{p-2} z$ is invertible, and therefore the optimal velocity has the potential form

$$v = -\|\nabla_x \Phi\|^{q-2} \nabla_x \Phi = -\nabla_\xi H_q(\nabla_x \Phi), \qquad H_q(\xi) = \frac{1}{q}\|\xi\|^q.$$

Thus, the potential parameterization used by PMOT is not an arbitrary assumption: it mirrors the velocity–multiplier relation in the smooth Benamou–Brenier optimality system. The Euler–Lagrange condition with respect to $\rho$ then yields $\partial_t \Phi + \nabla_x \Phi \cdot v + \frac{1}{p}\|v\|^p = 0$ and thus on the support of $\rho_t$ that

$$\partial_t \Phi - \frac{1}{q}\|\nabla \Phi\|^q = 0.$$

As we shall see, this corresponds to the fact that the velocity of a particle stays constant along its trajectory, a key feature of the OT. During neural training, $\Phi_\theta$ is a model parameter; it coincides with the BB multiplier only in the ideal zero-loss optimal regime, up to adding a function of time, which does not change $\nabla_x \Phi_\theta$ or the induced velocity.

### 2.3 Continuous Normalizing Flows

A Continuous Normalizing Flow defines an invertible map through an ordinary differential equation

$$\frac{dz_t}{dt} = v_\theta(t, z_t), \qquad z_0 = x.$$

Let $F_\theta$ denote the time-one flow map, $F_\theta(x) = z_1$. If the terminal density is chosen as a tractable prior, such as $\mathcal{N}(0, I)$, the data likelihood is computed by the instantaneous change-of-variables formula:

$$\frac{d}{dt} \log \rho_t(z_t) = -\nabla \cdot v_\theta(t, z_t).$$

Therefore,

$$\log \rho_0(x) = \log \rho_1(z_1) + \int_0^1 \nabla \cdot v_\theta(t, z_t)\, dt,$$

up to the sign convention determined by the integration direction. CNFs therefore provide likelihood evaluation while simultaneously defining a continuous transport trajectory.

## 3 Potential Matching Optimal Transport

We introduce *Potential Matching Optimal Transport* (PMOT), a variational framework for general $p$-cost optimal transport. PMOT parameterizes the CNF velocity field through a scalar potential and optimizes two terms: potential matching along model-generated straight bridges and terminal distribution matching. Under the assumptions stated below, every sufficiently regular zero-loss solution recovers the unique $p$-optimal Monge map and its corresponding Benamou–Brenier velocity field.

### 3.1 Potential-Induced Flow

Let $p > 1$ and $q = p/(p-1)$. Following the Benamou–Brenier optimality relation described above, we take a scalar potential $\Phi : [0, 1] \times \mathbb{R}^d \to \mathbb{R}$ as the primary variable and define the induced velocity field

$$v_\Phi(t, x) = -\|\nabla_x \Phi(t, x)\|^{q-2} \nabla_x \Phi(t, x). \tag{1}$$

For $p = 2$, equation 1 reduces to the familiar potential-flow relation $v_\Phi(t, x) = -\nabla_x \Phi(t, x)$.

For each $x \in \mathbb{R}^d$, consider the initial-value problem

$$\partial_t z(t) = v_\Phi\big(t, z(t)\big), \text{for almost every } t \in (0,1), \qquad z(0) = x. \tag{2}$$

Throughout, we restrict attention to potentials $\Phi$ such that, for every $x \in \mathbb{R}^d$, problem equation 2 admits a unique solution in $\mathrm{AC}([0,1];\mathbb{R}^d)$. We denote this solution by $z_\Phi(\cdot, x)$ and further require that the associated solution map $z_\Phi : [0,1] \times \mathbb{R}^d \to \mathbb{R}^d$ is jointly Borel measurable.

The terminal flow map $F_\Phi : \mathbb{R}^d \to \mathbb{R}^d$ is defined by

$$F_\Phi(x) = z_\Phi(1, x).$$

The distribution induced at time $t$ is

$$\rho_t^\Phi = \big(z_\Phi(t,\cdot)\big)_{\#}\mu_0.$$

In particular, $\rho_0^\Phi = \mu_0, \rho_1^\Phi = (F_\Phi)_{\#}\mu_0$.

### 3.2 The PMOT Variational Objective

The potential matching loss is defined by

$$\mathcal{L}_{\mathrm{PM}}(\Phi) := \mathbb{E}_{x\sim\mu_0}\left[\int_0^1 \Big\|\nabla_x \Phi(t,(1-t)x + tF_\Phi(x)) + \|F_\Phi(x) - x\|^{p-2}\,(F_\Phi(x) - x)\Big\|^2 \,\mathrm{d}t\right].$$

Let $\mathcal{D}$ be a nonnegative discrepancy between probability measures satisfying $\mathcal{D}(P,Q) = 0 \Leftrightarrow P = Q$. We define the terminal distribution loss by

$$\mathcal{L}_{\mathrm{term}}(\Phi) := \mathcal{D}(\rho_1^\Phi, \mu_1).$$

A principal example is the forward KL divergence, which gives $\mathcal{L}_{\mathrm{term}}(\Phi) = \mathrm{KL}(\rho_1^\Phi \| \mu_1)$.

We define the PMOT objective to be

$$\mathcal{L}_{\mathrm{PMOT}}(\Phi) := \lambda_{\mathrm{PM}}\mathcal{L}_{\mathrm{PM}}(\Phi) + \lambda_{\mathrm{term}}\mathcal{L}_{\mathrm{term}}(\Phi),$$

where $\lambda_{\mathrm{PM}}, \lambda_{\mathrm{term}} > 0$ are fixed weights. The domain $\mathrm{dom}(\mathcal{L}_{\mathrm{PMOT}})$ consists of all potentials $\Phi$ satisfying the preceding flow well-posedness and joint Borel-measurability requirements for which both $\mathcal{L}_{\mathrm{PM}}(\Phi)$ and $\mathcal{L}_{\mathrm{term}}(\Phi)$ are well defined.

*Remark* 3.1 (Velocity-space alternative). Potential matching loss may be replaced by the velocity residual

$$\big\|v_\Phi\big(t,(1-t)x + tF_\Phi(x)\big) - \big(F_\Phi(x) - x\big)\big\|^2.$$

The two formulations have the same zero set and coincide when $p = 2$. At finite loss, the nonlinear duality map changes their optimization conditioning. This suggests that velocity matching may sometimes be preferable for $p < 2$ and potential matching for $p > 2$, although neither uniformly dominates the other. We use potential matching as the default formulation throughout this work.

### 3.3 Zero Loss Implies Optimal Transport

Our main theorem is:

**Theorem 3.2** (Exact recovery and velocity-field uniqueness at zero loss)**.** *Let $p \in (1,\infty)$, let $\mu_0, \mu_1 \in \mathcal{P}_p(\mathbb{R}^d)$, and write $\mathrm{dom}(\mathcal{L}_{\mathrm{PMOT}})$ for the domain of the PMOT objective. Assume that $\mu_0$ is absolutely continuous with respect to Lebesgue measure. Assume that the $p$-Benamou–Brenier problem admits a minimizer $(\rho^\star, v^\star) = (\rho^{\Phi^\star}, v_{\Phi^\star})$ for some $\Phi^\star \in \mathrm{dom}(\mathcal{L}_{\mathrm{PMOT}})$. Then*

$$\min_{\Phi\in\mathrm{dom}(\mathcal{L}_{\mathrm{PMOT}})} \mathcal{L}_{\mathrm{PMOT}}(\Phi) = \mathcal{L}_{\mathrm{PMOT}}(\Phi^\star) = 0.$$

*Furthermore, let $\Phi$ be a global minimizer. If $\Phi \in C^2((0,1)\times\mathbb{R}^d)$, and if $\mathrm{supp}(\rho_t^\Phi) = \mathbb{R}^d$ for every $t \in (0,1)$, then $v_\Phi = v^\star$, $\mathrm{d}t\,\rho_t^\Phi(\mathrm{d}x)$-almost everywhere, and the corresponding terminal map $F_\Phi$ is the unique optimal Monge map from $\mu_0$ to $\mu_1$ for the cost $\|x-y\|^p$.*

Under the stated assumptions, this theorem provides the theoretical justification for PMOT: any sufficiently regular potential $\Phi$ attaining zero PMOT loss recovers the unique $p$-optimal Monge map and the corresponding Benamou–Brenier velocity field. Thus, in the ideal zero-loss setting, the PMOT objective exactly identifies the dynamic $p$-optimal transport solution. The proof is given in Appendix A.

*Remark* 3.3. The second part of Theorem 3.2 requires only interior regularity: $\Phi \in C^2((0,1)\times\mathbb{R}^d)$, with no regularity assumption at $t = 0$ or $t = 1$. The $C^2$ condition is imposed for simplicity; the proof also applies under weaker assumptions whenever the required weak derivatives, chain rules, and extension arguments remain valid. Moreover, the nondegeneracy of the support of $\rho_t^\Phi$ for $t \in (0,1)$ is essential for the minimizer to be the solution of OT. See Appendix A.2 for counterexamples.

### 3.4 Neural Parameterization and Training

For computation, we restrict the potential to a neural family $\{\Phi_\theta\}$ and use the scalar-valued ResNet potential architecture of OT-Flow (Onken et al., 2021). Let $g_\theta(t,x) = \nabla_x \Phi_\theta(t,x)$. The implementation uses the stabilized velocity

$$v_{\theta,\epsilon}(t,x) = -\big(\|g_\theta(t,x)\|^2 + \epsilon\big)^{(q-2)/2} g_\theta(t,x), \qquad \epsilon = 10^{-12}, \tag{3}$$

which approaches the population velocity in equation 1 as $\epsilon \to 0$. We write $v_\theta$ for $v_{\theta,\epsilon}$ below. The resulting ODE defines the flow $z_\theta(t,x)$ and terminal map $F_\theta(x) = z_\theta(1,x)$.

Given a minibatch $\{x_0^{(i)}\}_{i=1}^B$ from $\mu_0$, a forward ODE solve produces the model-induced endpoints $x_1^{(i)} = F_\theta(x_0^{(i)})$. For independently sampled $t_i \sim \mathcal{U}[0,1]$, define

$$\bar{x}_{t_i}^{(i)} = (1-t_i)x_0^{(i)} + t_i x_1^{(i)}, \qquad u^{(i)} = x_1^{(i)} - x_0^{(i)}.$$

Let

$$m_p(u) = \|u\|^{p-2}u, \qquad m_p(0) = 0,$$

denote the momentum dual to the $p$-power kinetic energy. The stochastic self-induced potential-matching loss is

$$\widehat{\mathcal{L}}_{\mathrm{PM}}(\theta) = \frac{1}{B}\sum_{i=1}^{B} \Big\| \nabla_x \Phi_\theta\big(t_i, \bar{x}_{t_i}^{(i)}\big) + m_p\big(u^{(i)}\big) \Big\|^2 . \tag{4}$$

The model-induced endpoints remain attached to the computational graph, so gradients propagate through $F_\theta$ in the potential-matching loss.

The population terminal objective remains

$$\mathcal{L}_{\mathrm{term}}(\theta) = \mathcal{D}\big((F_\theta)_{\#}\mu_0, \mu_1\big). \tag{5}$$

For likelihood-based training, we use the forward-KL discrepancy and optimize its equivalent CNF negative log-likelihood. Writing

$$\ell_\theta(x) = \int_0^1 \nabla \cdot v_\theta\big(t, z_\theta(t,x)\big)\,\mathrm{d}t,$$

the empirical NLL is

$$\widehat{\mathcal{L}}_{\mathrm{NLL}}(\theta) = -\frac{1}{B}\sum_{i=1}^{B}\Big[\log\varphi_1\big(F_\theta(x_0^{(i)})\big) + \ell_\theta(x_0^{(i)})\Big],$$

where $\varphi_1$ is the terminal reference density. The NLL differs from the forward-KL objective by a $\theta$-independent source-entropy constant. Therefore, the zero-loss statement in Theorem 3.2 refers to the population KL discrepancy, not to the numerical NLL value reported in experiments.

For sample-based terminal matching, we instead use a minibatch estimate of squared MMD between $\{F_\theta(x_0^{(i)})\}$ and independent samples from $\mu_1$ (Gretton et al., 2012).

In either case, the implemented objective is

$$\widehat{\mathcal{J}}_{\mathrm{PMOT}}(\theta) = \lambda_{\mathrm{PM}}\widehat{\mathcal{L}}_{\mathrm{PM}}(\theta) + \lambda_{\mathrm{term}}\widehat{\mathcal{L}}_{\mathrm{term}}(\theta). \tag{6}$$

No external OT pairs or HJB residual are used during training. We solve the dynamics using a differentiable fixed-step RK4 scheme and backpropagate through the ODE solve. Likelihood evaluation integrates data forward to the reference, whereas generation integrates reference samples backward to the data space.

Table 1: OT-geometry evaluation on 8-Gaussians and Pinwheel. PMOT endpoints are compared with post-hoc Sinkhorn barycentric references under the matching $p$-cost. Sinkhorn is used only for evaluation, with $\varepsilon = 0.02$ and 1000 iterations on 2000 samples. Ratios within a few percent of one indicate close agreement with the reference.

| Dataset | $p$ | PMOT $p$-cost | Sinkhorn $p$-cost | PMOT/Sinkhorn | Bary-MSE ↓ |
|---|---|---|---|---|---|
| 8-Gaussians | 1.5 | 2.104 | 2.107 | 0.999 | 0.0166 |
| | 2.0 | 2.671 | 2.732 | 0.978 | 0.0144 |
| | 3.0 | 4.554 | 4.668 | 0.976 | 0.0139 |
| Pinwheel | 1.5 | 0.770 | 0.767 | 1.004 | 0.0195 |
| | 2.0 | 0.725 | 0.719 | 1.007 | 0.0208 |
| | 3.0 | 0.658 | 0.636 | 1.034 | 0.0219 |

# 4 EXPERIMENTS

Our experiments are designed to evaluate three aspects of PMOT. First, we test whether PMOT endpoint maps agree with post-hoc OT references computed under the intended $p$-cost. Second, we examine whether the self-induced matching objective yields stable generation under mild likelihood weighting. Third, we evaluate whether PMOT remains competitive as a likelihood-based CNF on high-dimensional tabular density estimation. Across all experiments, Sinkhorn references are used only for evaluation and visualization, and never to construct training pairs.

## 4.1 TOY TRANSPORT GEOMETRY

Two-dimensional synthetic distributions provide a controlled setting in which post-hoc OT references can be estimated. For each exponent $p$, we compute an entropically regularized Sinkhorn coupling with $c_p(x, y) = \|x - y\|^p$ (Cuturi, 2013). Its transport cost and barycentric projection provide the reference cost and endpoint map, respectively; the resulting coupling and its derived quantities are used only post hoc for evaluation and visualization, never for training. We report the model-induced $p$-cost, its ratio to the reference cost, and endpoint MSE to the $p$-matched barycentric reference. Sinkhorn references are never used to construct training pairs. Additional unconditional generation results for the toy distributions are provided in Appendix B.1.

Table 1 gives the main quantitative geometry evaluation. On 8-Gaussians, all cost ratios are within $2.4\%$ of one. On Pinwheel, all ratios are within $3.4\%$ of one. Thus, when each model is evaluated against the matching exponent, its endpoint map has both transport cost and barycentric discrepancy close to the corresponding post-hoc OT reference.

To test whether the learned maps depend on the training exponent, we compare each checkpoint trained with $p_{\text{train}} \in \{1.5, 2, 3\}$ against barycentric reference maps computed with every $p_{\text{ref}} \in \{1.5, 2, 3\}$. Each entry in Figure 1 reports the corresponding endpoint MSE.

Figure 1 shows a diagonal preference: each PMOT checkpoint is closest to the reference computed with its training exponent. The separation is strongest between $p = 1.5$ and $p = 3$, while neighboring exponents remain closer on this smooth toy distribution. This supports $p$-specific behavior without requiring visually distinct trajectories.

Moons provides a complementary qualitative example in a less symmetric setting. Because entropic regularization can noticeably affect barycentric references on this dataset, we use this experiment only to visualize the learned coupling and continuous trajectories.

Figure 2 compares the PMOT-induced map with a post-hoc Sinkhorn reference and the continuous PMOT trajectories.

## 4.2 LIKELIHOOD-WEIGHT SENSITIVITY

We next compare PMOT with OT-Flow on 8-Gaussians under equal training budgets. PMOT uses only self-induced potential matching and likelihood, with weights $(\lambda_{\text{PM}}, \lambda_{\text{NLL}}) = (1, 1)$. OT-Flow

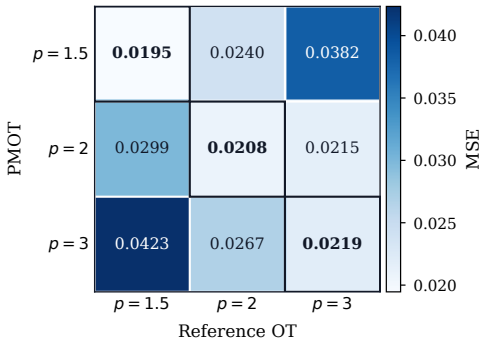



Figure 1: $p$-swap evaluation on Pinwheel. Rows correspond to PMOT checkpoints trained with exponent $p_{\text{train}}$, and columns correspond to post-hoc Sinkhorn barycentric reference maps computed with exponent $p_{\text{ref}}$. Each entry reports endpoint MSE for evaluation seed 0; lower is better. Bold entries mark the minimum in each row. Across five independently resampled evaluation batches with fixed checkpoints, the mean off-diagonal endpoint MSE is $1.41 \pm 0.05$ times the mean diagonal endpoint MSE.

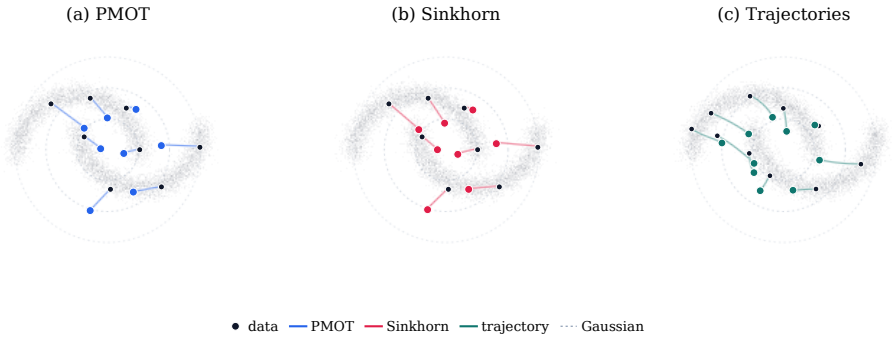



Figure 2: Learned transport geometry on two moons for $p = 2$. (a) Coupling induced by the PMOT map. (b) Post-hoc Sinkhorn barycentric reference. (c) Continuous PMOT trajectories. The resulting coupling and its derived quantities are used only post hoc for evaluation and visualization, never for training.

uses its standard kinetic, likelihood, and HJB/R objective; we fix the kinetic and HJB/R coefficients to one and vary only the likelihood coefficient. This comparison tests whether good generation quality requires a strongly likelihood-dominated objective.

Figure 3 shows the same effect visually under a shorter 1000-iteration budget: PMOT already recovers the eight modes clearly with balanced weights, whereas OT-Flow with $(1, 1, 1)$ exhibits stronger inter-mode artifacts. Table 2 quantifies the trend after 10k iterations. OT-Flow improves substantially as the likelihood coefficient is increased, whereas PMOT obtains the lowest histogram and MMD scores with the balanced $(1, 1)$ objective. This supports the view that the self-induced matching term provides useful transport structure without adding an HJB/R regularizer.

### 4.3 High-Dimensional Density Estimation

Table 3 compares PMOT and OT-Flow on MiniBooNE, POWER, and HEPMASS (Papamakarios et al., 2017; Grathwohl et al., 2018; Onken et al., 2021). PMOT uses the same $(1, 5)$ weighting across all three datasets and does not include an HJB/R regularizer, whereas OT-Flow uses dataset-specific likelihood and HJB/R coefficients. In the evaluated runs, PMOT obtains lower NLL on all three datasets. The $\text{MMD}^2$ comparison is dataset-dependent: PMOT is lower on POWER, while OT-

Table 2: Generation-quality comparison on 8-Gaussians. PMOT uses self-induced potential matching and likelihood weights $(\lambda_{\mathrm{PM}}, \lambda_{\mathrm{NLL}}) = (1, 1)$ and has no HJB/R regularizer. For OT-Flow, $(\lambda_L, \lambda_C, \lambda_R) = (1, w_C, 1)$ and only $w_C$ is varied. All models are trained for 10k iterations. Lower is better.

| Method | Weights | Hist JS ↓ | Hist L1 ↓ | MMD ↓ |
|---|---|---|---|---|
| PMOT | $(1, 1)$ | **0.0272** | **0.2863** | **0.00063** |
| OT-Flow | $(1, 1, 1)$ | 0.1006 | 0.6951 | 0.00725 |
| | $(1, 5, 1)$ | 0.0316 | 0.3259 | 0.00136 |
| | $(1, 10, 1)$ | 0.0303 | 0.3118 | 0.00108 |

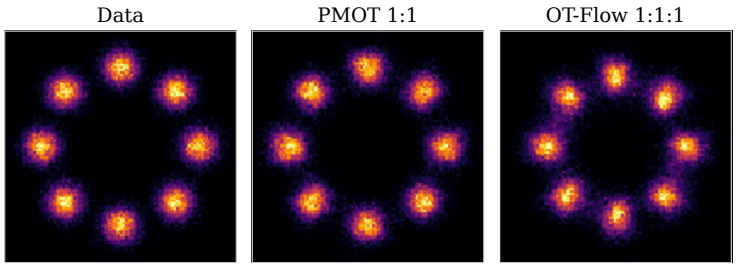



Figure 3: Generation quality on 8-Gaussians under a limited training budget of 1000 iterations. PMOT uses the mild balanced weights $(\lambda_{\mathrm{PM}}, \lambda_{\mathrm{NLL}}) = (1, 1)$, while OT-Flow uses $(\lambda_L, \lambda_C, \lambda_R) = (1, 1, 1)$. Under the same training budget and mild weighting, PMOT recovers the eight modes more clearly, while OT-Flow exhibits stronger inter-mode artifacts.

Flow is lower on MiniBooNE and HEPMASS. These results show that PMOT remains competitive for high-dimensional tabular density estimation with a simpler, fixed objective weighting.

**Image color transformation.** To illustrate sample-based terminal matching, we apply MMD-based PMOT to image color transformation. Figure 4 shows the transformation along the learned flow; experimental details and additional visualizations are provided in Appendix B.6.

## 5 Related Work

**CNFs and optimal-transport dynamics.** Continuous Normalizing Flows (CNFs) define invertible transformations through neural ordinary differential equations and evaluate likelihoods using the instantaneous change-of-variables formula (Chen et al., 2018; Grathwohl et al., 2018). This makes CNFs natural candidates for learning continuous transport maps, but likelihood maximization alone does not identify a unique path between the data distribution and the reference prior. OT-Flow addresses this ambiguity by combining a potential-flow CNF with kinetic-energy and HJB regularization, yielding dynamics closely related to the Benamou–Brenier formulation of quadratic-cost optimal transport (Benamou & Brenier, 2000; Onken et al., 2021; Jing & Li, 2025). Recent work has also used machine learning to approximate geodesic dynamics under related transport geometries, such as the spherical Wasserstein–Fisher–Rao metric (Jing et al., 2024). PMOT likewise learns continuous transport dynamics, but focuses on likelihood-based potential flows for general $p$-cost Wasserstein geometry (Villani, 2009; Peyré & Cuturi, 2019). It parameterizes the CNF velocity in the generalized Benamou–Brenier form for the chosen exponent $p$ and replaces the quadratic kinetic-energy regularizer with a self-induced potential-matching objective .

**Flow matching and neural OT with general costs.** Flow matching trains continuous-time generative models by regressing velocity fields along prescribed probability paths, avoiding the need to backpropagate through ODE solves during training (Lipman et al., 2023). OT-coupled flow-matching methods use minibatch OT couplings to define training pairs or conditional paths (Tong

Table 3: High-dimensional tabular density estimation for $p = 2$. Weights are $(\lambda_{\mathrm{PM}}, \lambda_{\mathrm{NLL}})$ for PMOT and $(\lambda_L, \lambda_C, \lambda_R)$ for OT-Flow. NLL is from one training run; $\mathrm{MMD}^2$ is the mean over 20 paired large-sample evaluations (Appendix B.5). Lower is better.

| Dataset | Method | Weights | NLL ↓ | $\mathrm{MMD}^2$ ($\times 10^{-4}$) ↓ |
|---|---|---|---|---|
| MiniBooNE | PMOT | $(1, 5)$ | 10.454 | 1.402 |
| | OT-Flow | $(1, 100, 15)$ | 10.634 | 0.658 |
| POWER | PMOT | $(1, 5)$ | -0.383 | 0.106 |
| | OT-Flow | $(1, 500, 5)$ | -0.312 | 1.069 |
| HEPMASS | PMOT | $(1, 5)$ | 16.922 | 0.343 |
| | OT-Flow | $(1, 500, 40)$ | 17.351 | 0.093 |

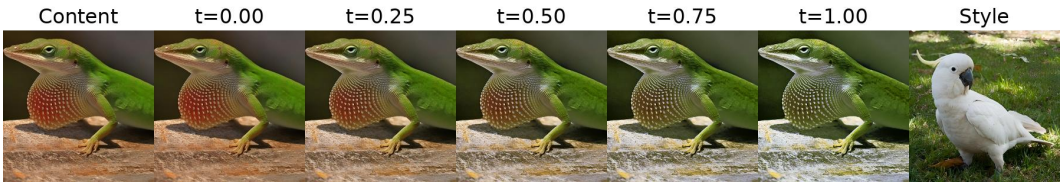



Figure 4: MMD-based image color transformation along the learned PMOT flow. The leftmost panel is the source image and the rightmost panel is the target style image.

et al., 2023). PMOT instead uses a potential matching residual whose endpoint pair is induced by the current CNF map, so no external OT coupling is used during training. Neural OT methods also learn maps or couplings under general cost functions, including costs beyond the quadratic case (Korotin et al., 2023; Asadulaev et al., 2024). PMOT is complementary to this literature: rather than learning only a static map or using minibatch OT pairs as supervision, it learns continuous potential-flow dynamics while preserving CNF likelihood evaluation and allowing flexible terminal matching such as KL/NLL or MMD.

## 6 Conclusion

We presented Potential Matching Optimal Transport (PMOT), a potential-flow CNF framework for general $p$-cost optimal transport. PMOT parameterizes the CNF velocity field with a scalar potential in the generalized Benamou–Brenier form and trains the potential gradient using a self-induced matching loss on straight bridges determined by the model endpoints. It requires no external transport pairs or inner OT optimization and supports both likelihood-based training through a KL/NLL terminal objective and sample-based terminal matching through MMD.

Our main result establishes exactness at zero population PMOT loss: under the stated realizability, regularity, and full-support assumptions, every global minimizer recovers the unique $p$-optimal Monge map and its Benamou–Brenier dynamics. On synthetic benchmarks, the learned maps agree with $p$-matched OT references and are closest to the references computed using their respective training exponents. PMOT also remains competitive as a likelihood-based density model on high-dimensional tabular data, while an additional MMD-based color transformation experiment demonstrates sample-based terminal matching. As with deterministic CNFs more broadly, PMOT represents Monge-type maps, and finite-sample training, numerical integration, and optimization introduce practical approximation errors.

## Reproducibility Statement

The model parameterization, training objectives, and experimental procedures are described in Sections 3 and 4. Appendix A provides the assumptions and complete proofs for the theoretical results. Appendix B reports the dataset preprocessing, model architectures, optimization and numerical integration settings, checkpoint selection procedures, and evaluation protocols. We also distinguish

results obtained from single training runs from repeated evaluations of fixed checkpoints. These details are provided to support independent reproduction of the theoretical and empirical results.

## AI USE STATEMENT

OpenAI Codex (GPT-5) was used to assist with polishing the language and organization of the manuscript, drafting and revising portions of the text, checking consistency between the experimental descriptions and reported results, and reviewing and modifying the code used for the MMD evaluation. The authors reviewed and revised the AI-assisted text and code as needed, and verified the reported results against the experiment outputs. The authors take full responsibility for the final content of the paper, including all AI-assisted text, code, analyses, and results.

## REFERENCES

Arip Asadulaev, Alexander Korotin, Vage Egiazarian, Petr Mokrov, and Evgeny Burnaev. Neural optimal transport with general cost functionals. In *International Conference on Learning Representations*, 2024. URL https://openreview.net/forum?id=gIiz7tBtYZ.

Jean-David Benamou and Yann Brenier. A computational fluid mechanics solution to the monge-kantorovich mass transfer problem. *Numerische Mathematik*, 84(3):375–393, 2000. doi: 10.1007/s002110050002.

Ricky TQ Chen, Yulia Rubanova, Jesse Bettencourt, and David K Duvenaud. Neural ordinary differential equations. *Advances in neural information processing systems*, 31, 2018.

Marco Cuturi. Sinkhorn distances: Lightspeed computation of optimal transport. In *Advances in Neural Information Processing Systems*, 2013.

Jia Deng, Wei Dong, Richard Socher, Li-Jia Li, Kai Li, and Li Fei-Fei. Imagenet: A large-scale hierarchical image database. In *2009 IEEE Conference on Computer Vision and Pattern Recognition*, pp. 248–255, 2009. doi: 10.1109/CVPR.2009.5206848.

Will Grathwohl, Ricky TQ Chen, Jesse Bettencourt, Ilya Sutskever, and David Duvenaud. Ffjord: Free-form continuous dynamics for scalable reversible generative models. *arXiv preprint arXiv:1810.01367*, 2018.

Arthur Gretton, Karsten M. Borgwardt, Malte J. Rasch, Bernhard Schölkopf, and Alexander Smola. A kernel two-sample test. *Journal of Machine Learning Research*, 13(25):723–773, 2012. URL https://www.jmlr.org/papers/v13/gretton12a.html.

Yang Jing and Lei Li. Convergence analysis of ot-flow for sample generation. *Numerical Mathematics: Theory, Methods and Applications*, 18(2):325–352, 2025.

Yang Jing, Jiaheng Chen, Lei Li, and Jianfeng Lu. A machine learning framework for geodesics under spherical wasserstein–fisher–rao metric and its application for weighted sample generation. *Journal of Scientific Computing*, 98(1):5, 2024.

Alexander Korotin, Daniil Selikhanovych, and Evgeny Burnaev. Neural optimal transport. In *International Conference on Learning Representations*, 2023. URL https://openreview.net/forum?id=d8CBRlWNkqH.

Yaron Lipman, Ricky T. Q. Chen, Heli Ben-Hamu, Maximilian Nickel, and Matt Le. Flow matching for generative modeling. In *International Conference on Learning Representations*, 2023. URL https://openreview.net/forum?id=PqvMRDCJT9t.

Derek Onken, Samy Wu Fung, Xingjian Li, and Lars Ruthotto. OT-Flow: Fast and accurate continuous normalizing flows via optimal transport. In *Proceedings of the AAAI Conference on Artificial Intelligence*, volume 35, pp. 9223–9232, 2021. doi: 10.1609/aaai.v35i10.17113. URL https://ojs.aaai.org/index.php/AAAI/article/view/17113.

George Papamakarios, Theo Pavlakou, and Iain Murray. Masked autoregressive flow for density estimation. In *Advances in Neural Information Processing Systems*, 2017.

Gabriel Peyré and Marco Cuturi. Computational optimal transport. *Foundations and Trends in Machine Learning*, 11(5–6):355–607, 2019. doi: 10.1561/2200000073.

Olga Russakovsky, Jia Deng, Hao Su, Jonathan Krause, Sanjeev Satheesh, Sean Ma, Zhiheng Huang, Andrej Karpathy, Aditya Khosla, Michael Bernstein, Alexander C. Berg, and Li Fei-Fei. ImageNet Large Scale Visual Recognition Challenge. *International Journal of Computer Vision (IJCV)*, 115(3):211–252, 2015. doi: 10.1007/s11263-015-0816-y.

Filippo Santambrogio. *Optimal Transport for Applied Mathematicians: Calculus of Variations, PDEs, and Modeling*, volume 87 of *Progress in Nonlinear Differential Equations and Their Applications*. Birkhäuser Cham, 2015. doi: 10.1007/978-3-319-20828-2.

Alexander Tong, Kilian Fatras, Nikolay Malkin, Guillaume Huguet, Yanlei Zhang, Jarrid Rector-Brooks, Guy Wolf, and Yoshua Bengio. Improving and generalizing flow-based generative models with minibatch optimal transport. *arXiv preprint arXiv:2302.00482*, 2023.

Cédric Villani. *Optimal transport: old and new*, volume 338. Springer, 2009.

# A Details for Theorem 3.2

## A.1 Proof of Theorem 3.2

*Proof.* (1) By assumption, $(\rho^\star, v^\star) = (\rho^{\Phi^\star}, v_{\Phi^\star})$ is a solution of the $p$-Benamou–Brenier problem for some $\Phi^\star \in \mathrm{dom}(\mathcal{L}_{\mathrm{PMOT}})$.

The endpoint condition of the Benamou–Brenier problem and the definition of the induced flow give

$$(F_{\Phi^\star})_\sharp \mu_0 = \rho_1^{\Phi^\star} = \rho_1^\star = \mu_1.$$

Since $(\rho^{\Phi^\star}, v_{\Phi^\star})$ minimizes the Benamou–Brenier action, the pushforward formula and the characteristic equation yield

$$\begin{aligned}
\frac{1}{p} W_p^p(\mu_0, \mu_1) &= \frac{1}{p} \int_0^1 \int_{\mathbb{R}^d} \|v_{\Phi^\star}(t,y)\|^p \, \rho_t^{\Phi^\star}(\mathrm{d}y)\, \mathrm{d}t \\
&= \frac{1}{p} \int_{\mathbb{R}^d} \int_0^1 \|\partial_t z_{\Phi^\star}(t,x)\|^p \, \mathrm{d}t \, \mu_0(\mathrm{d}x) \\
&\geq \frac{1}{p} \int_{\mathbb{R}^d} \|F_{\Phi^\star}(x) - x\|^p \, \mu_0(\mathrm{d}x) \\
&\geq \frac{1}{p} W_p^p(\mu_0, \mu_1).
\end{aligned}$$

The first inequality is Jensen's inequality applied to $\mu_0$-almost every trajectory of finite $p$-energy, using

$$F_{\Phi^\star}(x) - x = \int_0^1 \partial_t z_{\Phi^\star}(t,x)\, \mathrm{d}t,$$

and the second follows because $(\mathrm{Id}, F_{\Phi^\star})_\sharp \mu_0 \in \Pi(\mu_0, \mu_1)$. Since the leftmost and rightmost quantities in the preceding chain coincide, equality holds throughout. In particular, $(\mathrm{Id}, F_{\Phi^\star})_\sharp \mu_0$ is an optimal coupling. Since $\mu_0$ is absolutely continuous and $p > 1$, the optimal coupling is induced by the unique optimal Monge map $T_p$, and therefore

$$F_{\Phi^\star} = T_p \qquad \mu_0\text{-almost everywhere.}$$

Moreover, the nonnegative gap in Jensen's inequality has zero integral with respect to $\mu_0$. Thus equality in Jensen's inequality holds for $\mu_0$-almost every $x$. Since $w \mapsto \|w\|^p$ is strictly convex for $p > 1$, this implies

$$\partial_t z_{\Phi^\star}(t,x) = F_{\Phi^\star}(x) - x \qquad \text{for almost every } t \in (0,1)$$

for $\mu_0$-almost every $x$. Since $z_{\Phi^\star}(\cdot, x)$ is absolutely continuous and $z_{\Phi^\star}(0,x) = x$, integration in time gives

$$z_{\Phi^\star}(t,x) = (1-t)x + tF_{\Phi^\star}(x) = (1-t)x + tT_p(x)$$

for every $t \in [0,1]$ and for $\mu_0$-almost every $x$. Combining this identity with the characteristic equation gives

$$v_{\Phi^\star}\big(t,(1-t)x+tF_{\Phi^\star}(x)\big) = F_{\Phi^\star}(x)-x \qquad \mathrm{d}t\otimes\mu_0\text{-almost everywhere.}$$

For $r>1$, let $A_r(\xi) := \|\xi\|^{r-2}\xi$, with $A_r(0) := 0$. The duality maps $A_p$ and $A_q$ are odd and inverse to each other. Since $v_{\Phi^\star} = -A_q(\nabla_x\Phi^\star)$, the preceding velocity identity is equivalent to

$$\nabla_x\Phi^\star\big(t,(1-t)x+tF_{\Phi^\star}(x)\big) = -\|F_{\Phi^\star}(x)-x\|^{p-2}\big(F_{\Phi^\star}(x)-x\big) \qquad \mathrm{d}t\otimes\mu_0\text{-almost everywhere.}$$

Thus the potential-matching residual vanishes and $\mathcal{L}_{\mathrm{PM}}(\Phi^\star)=0$. The endpoint identity above also gives $\mathcal{L}_{\mathrm{term}}(\Phi^\star)=0$. Since the two terms in the PMOT objective are nonnegative and have positive weights,

$$\min_{\Phi\in\mathrm{dom}(\mathcal{L}_{\mathrm{PMOT}})} \mathcal{L}_{\mathrm{PMOT}}(\Phi) = \mathcal{L}_{\mathrm{PMOT}}(\Phi^\star) = 0.$$

(2) Now let $\Phi$ be a global minimizer satisfying the regularity and full-support assumptions of the theorem. By part (1), the minimum value of the PMOT objective is zero. Hence

$$\mathcal{L}_{\mathrm{PM}}(\Phi) = \mathcal{L}_{\mathrm{term}}(\Phi) = 0,$$

and in particular, $(F_\Phi)_\#\mu_0 = \mu_1$.

Define

$$S_t(x) := (1-t)x + tF_\Phi(x)$$

and the potential-matching residual

$$R(t,x) := \nabla_x\Phi\big(t,S_t(x)\big) + \|F_\Phi(x)-x\|^{p-2}\big(F_\Phi(x)-x\big), \qquad (t,x)\in(0,1)\times\mathbb{R}^d.$$

Since the solution map $z_\Phi$ is jointly Borel measurable, its terminal-time slice $F_\Phi = z_\Phi(1,\cdot)$ is Borel measurable. Consequently, the map $(t,x)\mapsto S_t(x)$ is jointly Borel measurable. Moreover, $\nabla_x\Phi$ is continuous on $(0,1)\times\mathbb{R}^d$, and the map $\xi\mapsto\|\xi\|^{p-2}\xi$, with value 0 at $\xi=0$, is continuous for $p>1$. It follows that $R$ is jointly Borel measurable.

The function $(t,x)\mapsto\|R(t,x)\|^2$ is therefore nonnegative and jointly Borel measurable. By Tonelli's theorem, the function

$$h(x) := \int_0^1 \|R(t,x)\|^2\,\mathrm{d}t$$

is measurable. Since $\mathcal{L}_{\mathrm{PM}}(\Phi)=0$,

$$0 = \int_{\mathbb{R}^d} h(x)\,\mu_0(\mathrm{d}x).$$

Because $h\geq 0$, it follows that $h=0$ for $\mu_0$-almost every $x$. Hence the measurable set

$$E := \{x\in\mathbb{R}^d : h(x)=0\}$$

satisfies $\mu_0(E)=1$. For every $x\in E$, we have

$$\int_0^1 \|R(t,x)\|^2\,\mathrm{d}t = 0,$$

and therefore

$$R(t,x)=0 \qquad \text{for almost every } t\in(0,1).$$

For each fixed $x\in E$, the map $t\mapsto R(t,x)$ is continuous on $(0,1)$. Since it vanishes for almost every $t\in(0,1)$, it must vanish for every $t\in(0,1)$.

Thus, for every $x\in E$ and $t\in(0,1)$,

$$\nabla_x\Phi\big(t,S_t(x)\big) = -A_p\big(F_\Phi(x)-x\big).$$

Using $v_\Phi = -A_q(\nabla_x\Phi)$, together with the oddness and inverse relation of the duality maps defined in part (1), gives

$$v_\Phi\big(t,S_t(x)\big) = -A_q\big(-A_p(F_\Phi(x)-x)\big) = F_\Phi(x)-x.$$

Since

$$\partial_t S_t(x) = F_\Phi(x) - x,$$

it follows that, for every $x \in E$,

$$\partial_t S_t(x) = v_\Phi\big(t, S_t(x)\big), \qquad t \in (0,1), \qquad S_0(x) = x.$$

Since $S_\cdot(x)$ is affine in time, it is absolutely continuous on $[0,1]$ and satisfies the characteristic equation on $(0,1)$. Hence $S_\cdot(x)$ solves problem equation 2, and uniqueness gives

$$z_\Phi(t,x) = S_t(x) \qquad \text{for every } t \in [0,1] \text{ and every } x \in E.$$

In particular,

$$v_\Phi\big(t, z_\Phi(t,x)\big) = F_\Phi(x) - x \qquad \text{for every } t \in (0,1) \text{ and every } x \in E.$$

Thus, for $\mu_0$-almost every initial point, the induced trajectory is a constant-speed straight line and the velocity is constant along it.

It remains to show that the pair $(\rho_t^\Phi, v_\Phi)$ induced by these straight-line trajectories is a minimizer of the $p$-Benamou–Brenier problem. We first prove that $F_\Phi$ is the optimal map for the static $p$-cost transport problem and then verify that the induced straight-line flow attains the minimum Benamou–Brenier action. Set

$$Q := (0,1) \times \mathbb{R}^d, \qquad q = \frac{p}{p-1}, \qquad H_q(\xi) = \frac{1}{q}\|\xi\|^q, \qquad A_q(\xi) = \nabla H_q(\xi) = \|\xi\|^{q-2}\xi,$$

and write $g = \nabla_x \Phi$, so that $v_\Phi = -A_q(g)$. Define

$$G(t,x) := \partial_t \Phi(t,x) - H_q(g(t,x)), \qquad (t,x) \in Q.$$

We claim that $\nabla_x G = 0$ on $Q$. Since $\Phi \in C^2(Q)$, the field $g = \nabla_x \Phi$ is $C^1$ on $Q$. Moreover, for every $q > 1$, the map $A_q(\xi) = \|\xi\|^{q-2}\xi$ is $C^1$ on $\mathbb{R}^d \setminus \{0\}$, with

$$DA_q(\xi) = \|\xi\|^{q-2} I + (q-2)\|\xi\|^{q-4}\xi \otimes \xi.$$

Since $g$ is continuous, the set

$$U := \{(t,x) \in Q : g(t,x) \neq 0\}$$

is open. Therefore, $v_\Phi = -A_q \circ g$ is $C^1$ on $U$ by the chain rule. For every $x \in E$, the velocity is constant along the corresponding characteristic:

$$v_\Phi\big(t, z_\Phi(t,x)\big) = F_\Phi(x) - x, \qquad t \in (0,1).$$

By the straight-line identity, $z_\Phi(\cdot, x) = S_\cdot(x)$ is affine and therefore $C^1$ on $(0,1)$. Since $U$ is open and $z_\Phi(\cdot,x)$ is continuous, whenever $x \in E$ and $(t, z_\Phi(t,x)) \in U$, the trajectory remains in $U$ on a neighborhood of $t$. The $C^1$ chain rule therefore applies on this neighborhood, and differentiating the preceding identity with respect to $t$ and using $\partial_t z_\Phi(t,x) = v_\Phi(t, z_\Phi(t,x))$ gives

$$\begin{aligned} 0 &= \frac{\mathrm{d}}{\mathrm{d}t} v_\Phi\big(t, z_\Phi(t,x)\big) \\ &= \partial_t v_\Phi\big(t, z_\Phi(t,x)\big) + D_x v_\Phi\big(t, z_\Phi(t,x)\big)\, \partial_t z_\Phi(t,x) \\ &= \big[\partial_t v_\Phi + D_x v_\Phi\, v_\Phi\big]\big(t, z_\Phi(t,x)\big). \end{aligned}$$

Define the space–time measure as the pushforward

$$\nu := \big((t,x) \mapsto (t, z_\Phi(t,x))\big)_{\#}\big(\mathrm{d}t \otimes \mu_0\big).$$

The joint Borel measurability of $z_\Phi$ ensures that this measure is well defined. Since $\rho_t^\Phi = (z_\Phi(t,\cdot))_{\#}\mu_0$, it can equivalently be written as

$$\nu(\mathrm{d}t, \mathrm{d}y) = \mathrm{d}t\, \rho_t^\Phi(\mathrm{d}y).$$

Since $\mu_0(E) = 1$, the preceding identity implies

$$\partial_t v_\Phi + D_x v_\Phi\, v_\Phi = 0 \qquad \nu\text{-almost everywhere on } U.$$

The assumption $\operatorname{supp}(\rho_t^\Phi) = \mathbb{R}^d$ for every $t \in (0,1)$ implies that $\nu$ has full support on $Q$. Indeed, every nonempty open subset of $Q$ contains a product $I \times B$, where $I \subset (0,1)$ and $B \subset \mathbb{R}^d$ are nonempty and open, and

$$\nu(I \times B) = \int_I \rho_t^\Phi(B)\,\mathrm{d}t > 0.$$

Since the map

$$(t,x) \longmapsto \partial_t v_\Phi(t,x) + D_x v_\Phi(t,x) v_\Phi(t,x)$$

is continuous on $U$, it follows that

$$(\partial_t + v_\Phi \cdot \nabla_x) v_\Phi = \partial_t v_\Phi + D_x v_\Phi\, v_\Phi = 0 \qquad \text{on } U.$$

To relate the material derivative of $v_\Phi$ to $\nabla_x G$, note that $D_x g = D_x^2 \Phi$, $DA_q = D^2 H_q$, and $(v_\Phi \cdot \nabla_x) v_\Phi = D_x v_\Phi\, v_\Phi$. Hence, the chain rule yields

$$\begin{aligned}(\partial_t + v_\Phi \cdot \nabla_x) v_\Phi &= \partial_t v_\Phi + D_x v_\Phi\, v_\Phi \\ &= -DA_q(g)\,\partial_t g - DA_q(g) D_x g\, v_\Phi \\ &= -D^2 H_q(g)\big(\partial_t g + D_x^2 \Phi\, v_\Phi\big).\end{aligned}$$

On the other hand, using the symmetry of $D_x^2\Phi$ and $v_\Phi = -A_q(g)$,

$$\begin{aligned}\nabla_x G &= \partial_t g - \nabla_x\big(H_q(g)\big) \\ &= \partial_t g - (D_x g)^\top A_q(g) \\ &= \partial_t g - D_x^2 \Phi\, A_q(g) \\ &= \partial_t g + D_x^2 \Phi\, v_\Phi.\end{aligned}$$

Combining the preceding two identities yields

$$0 = (\partial_t + v_\Phi \cdot \nabla_x) v_\Phi = -D^2 H_q(g) \nabla_x G \qquad \text{on } U.$$

For $g \neq 0$,

$$D^2 H_q(g) = \|g\|^{q-2} I + (q-2)\|g\|^{q-4} g \otimes g$$

is positive definite. Indeed, for any $\eta \in \mathbb{R}^d$, define its components parallel and orthogonal to $g$ by

$$\eta_\parallel := \frac{\eta \cdot g}{\|g\|^2} g, \qquad \eta_\perp := \eta - \eta_\parallel.$$

Then $\eta = \eta_\perp + \eta_\parallel$, $\eta_\perp \cdot g = 0$, and $(g \cdot \eta)^2 = \|g\|^2 \|\eta_\parallel\|^2$. Hence

$$\begin{aligned}\eta^\top D^2 H_q(g) \eta &= \|g\|^{q-2}\|\eta\|^2 + (q-2)\|g\|^{q-4}(g \cdot \eta)^2 \\ &= \|g\|^{q-2}\big(\|\eta_\perp\|^2 + \|\eta_\parallel\|^2 + (q-2)\|\eta_\parallel\|^2\big) \\ &= \|g\|^{q-2}\big(\|\eta_\perp\|^2 + (q-1)\|\eta_\parallel\|^2\big) > 0\end{aligned}$$

for every $\eta \neq 0$, since $g \neq 0$ and $q > 1$. Equivalently, the tangential eigenvalue is $\|g\|^{q-2}$ and the radial eigenvalue is $(q-1)\|g\|^{q-2}$. Therefore $\nabla_x G = 0$ on $U$.

It remains to consider the zero set

$$Z := \{(t,x) \in Q : g(t,x) = 0\}.$$

At every interior point of $Z$ relative to $Q$, the field $g$ vanishes in a neighborhood, so $\partial_t g = 0$ there and hence $\nabla_x G = 0$. Every other point of $Z$ is a limit point of $U$, and the continuity on $Q$ of

$$\nabla_x G = \partial_t g - D_x^2 \Phi\, A_q(g)$$

again yields $\nabla_x G = 0$. Thus $\nabla_x G = 0$ on $Z$ as well. Together with the conclusion on $U$, this yields

$$\nabla_x G = 0 \qquad \text{on } Q.$$

Since $\mathbb{R}^d$ is connected, there is a continuous function $a : (0,1) \to \mathbb{R}$ such that

$$G(t,x) = a(t) \qquad (t,x) \in Q.$$

Define

$$\alpha(t) := \int_{1/2}^{t} a(s)\,\mathrm{d}s, \qquad t \in (0,1).$$

Then $\alpha'(t) = a(t)$ on $(0,1)$. The gauge-adjusted potential

$$\widetilde{\Phi}(t,x) := \Phi(t,x) - \alpha(t)$$

induces the same velocity on $(0,1) \times \mathbb{R}^d$, and satisfies the Hamilton–Jacobi equation

$$\partial_t \widetilde{\Phi} = H_q(\nabla_x \widetilde{\Phi}) \qquad \text{on } Q.$$

Let $c_p(x,y) = \|x-y\|^p/p$. Fenchel's inequality, applied to the convex conjugate pair $L_p(w) = \|w\|^p/p$ and $H_q(\xi) = \|\xi\|^q/q$, reads

$$L_p(w) + H_q(\xi) + w \cdot \xi \geq 0,$$

with equality if and only if $w = -A_q(\xi)$. Fix $0 < \varepsilon < 1/2$. For every $x \in E$,

$$F_\Phi(x) - x = -A_q\big(\nabla_x \widetilde{\Phi}(t, S_t(x))\big), \qquad t \in (0,1),$$

so equality holds in Fenchel's inequality along the straight-line trajectory $S_t(x)$. Since $\partial_t S_t(x) = F_\Phi(x) - x$, the chain rule and the Hamilton–Jacobi equation give

$$\begin{aligned}
\frac{\mathrm{d}}{\mathrm{d}t}\widetilde{\Phi}\big(t, S_t(x)\big) &= \partial_t \widetilde{\Phi}\big(t, S_t(x)\big) + \nabla_x \widetilde{\Phi}\big(t, S_t(x)\big) \cdot \partial_t S_t(x) \\
&= H_q\big(\nabla_x \widetilde{\Phi}(t, S_t(x))\big) + \nabla_x \widetilde{\Phi}\big(t, S_t(x)\big) \cdot \big(F_\Phi(x) - x\big) \\
&= -L_p\big(F_\Phi(x) - x\big) \\
&= -c_p\big(x, F_\Phi(x)\big).
\end{aligned}$$

Therefore, the fundamental theorem of calculus on $[\varepsilon, 1-\varepsilon]$ yields

$$\begin{aligned}
&\widetilde{\Phi}\big(1-\varepsilon, S_{1-\varepsilon}(x)\big) - \widetilde{\Phi}\big(\varepsilon, S_\varepsilon(x)\big) \\
&\quad = \int_\varepsilon^{1-\varepsilon} \frac{\mathrm{d}}{\mathrm{d}t}\widetilde{\Phi}\big(t, S_t(x)\big)\,\mathrm{d}t = -(1-2\varepsilon) c_p\big(x, F_\Phi(x)\big).
\end{aligned}$$

Equivalently,

$$\widetilde{\Phi}\big(\varepsilon, S_\varepsilon(x)\big) - \widetilde{\Phi}\big(1-\varepsilon, S_{1-\varepsilon}(x)\big) = (1-2\varepsilon) c_p\big(x, F_\Phi(x)\big) = \frac{\|S_{1-\varepsilon}(x) - S_\varepsilon(x)\|^p}{p(1-2\varepsilon)^{p-1}}.$$

Take finitely many points $x_1, \ldots, x_N \in E$, set $y_i := F_\Phi(x_i)$, and let $\sigma$ be any permutation of $\{1, \ldots, N\}$. For each $i$, define the constant-speed line

$$\gamma_i(t) := S_\varepsilon(x_i) + \frac{t-\varepsilon}{1-2\varepsilon}\left(S_{1-\varepsilon}(x_{\sigma(i)}) - S_\varepsilon(x_i)\right), \qquad t \in [\varepsilon, 1-\varepsilon].$$

Its velocity is

$$\partial_t \gamma_i(t) = \frac{S_{1-\varepsilon}(x_{\sigma(i)}) - S_\varepsilon(x_i)}{1-2\varepsilon}.$$

By the chain rule, the Hamilton–Jacobi equation, and Fenchel's inequality,

$$\frac{\mathrm{d}}{\mathrm{d}t}\widetilde{\Phi}\big(t, \gamma_i(t)\big) = H_q\big(\nabla_x \widetilde{\Phi}(t, \gamma_i(t))\big) + \nabla_x \widetilde{\Phi}(t, \gamma_i(t)) \cdot \partial_t \gamma_i(t) \geq -L_p\big(\partial_t \gamma_i(t)\big).$$

Integrating over $[\varepsilon, 1-\varepsilon]$ and using the fact that $\partial_t \gamma_i$ is constant gives

$$\widetilde{\Phi}\big(\varepsilon, S_\varepsilon(x_i)\big) - \widetilde{\Phi}\big(1-\varepsilon, S_{1-\varepsilon}(x_{\sigma(i)})\big) \leq (1-2\varepsilon) L_p\big(\partial_t \gamma_i\big) = \frac{\|S_{1-\varepsilon}(x_{\sigma(i)}) - S_\varepsilon(x_i)\|^p}{p(1-2\varepsilon)^{p-1}}.$$

The preceding equality, invariance of the sum of the terminal potential values under permutation, and these cross-pair inequalities give

$$\begin{aligned}\sum_{i=1}^{N} \frac{\|S_{1-\varepsilon}(x_i) - S_{\varepsilon}(x_i)\|^p}{p(1-2\varepsilon)^{p-1}} &= \sum_{i=1}^{N} \Big[\widetilde{\Phi}\big(\varepsilon, S_{\varepsilon}(x_i)\big) - \widetilde{\Phi}\big(1-\varepsilon, S_{1-\varepsilon}(x_i)\big)\Big] \\ &= \sum_{i=1}^{N} \Big[\widetilde{\Phi}\big(\varepsilon, S_{\varepsilon}(x_i)\big) - \widetilde{\Phi}\big(1-\varepsilon, S_{1-\varepsilon}(x_{\sigma(i)})\big)\Big] \\ &\leq \sum_{i=1}^{N} \frac{\|S_{1-\varepsilon}(x_{\sigma(i)}) - S_{\varepsilon}(x_i)\|^p}{p(1-2\varepsilon)^{p-1}}.\end{aligned}$$

As $\varepsilon \to 0^+$,

$$S_{\varepsilon}(x_i) \longrightarrow x_i, \qquad S_{1-\varepsilon}(x_i) \longrightarrow y_i.$$

Taking the limit in the preceding finite-sum inequality yields

$$\sum_{i=1}^{N} c_p(x_i, y_i) \leq \sum_{i=1}^{N} c_p(x_i, y_{\sigma(i)}).$$

Therefore,

$$\Gamma := \{(x, F_{\Phi}(x)) : x \in E\}$$

is $c_p$-cyclically monotone. Since $\mathcal{L}_{\mathrm{term}}(\Phi) = 0$, the measure

$$\pi_{\Phi} := (\mathrm{Id}, F_{\Phi})_{\#}\mu_0$$

belongs to $\Pi(\mu_0, \mu_1)$ and is concentrated on $\Gamma$. Moreover,

$$\begin{aligned}\int_{\mathbb{R}^d \times \mathbb{R}^d} c_p(x,y)\, \pi_{\Phi}(\mathrm{d}x, \mathrm{d}y) &= \frac{1}{p} \int_{\mathbb{R}^d} \|F_{\Phi}(x) - x\|^p \, \mu_0(\mathrm{d}x) \\ &\leq \frac{2^{p-1}}{p} \left( \int_{\mathbb{R}^d} \|x\|^p \, \mu_0(\mathrm{d}x) + \int_{\mathbb{R}^d} \|y\|^p \, \mu_1(\mathrm{d}y) \right) < \infty.\end{aligned}$$

Since $c_p$ is continuous and finite-valued on $\mathbb{R}^d \times \mathbb{R}^d$, and $\pi_{\Phi}$ has finite $c_p$-cost, the standard sufficiency theorem for $c_p$-cyclically monotone transport plans implies that $\pi_{\Phi}$ is an optimal coupling (Santambrogio, 2015). The factor $1/p$ does not affect the optimizer, so $F_{\Phi}$ is optimal for the cost $\|x - y\|^p$.

Since $\mu_0$ is absolutely continuous and $p > 1$, the optimal transport map for this cost is unique $\mu_0$-almost everywhere. Consequently,

$$F_{\Phi} = T_p \qquad \mu_0\text{-almost everywhere.}$$

We now verify the dynamic optimality explicitly. Since $\rho_t^{\Phi} = (z_{\Phi}(t, \cdot))_{\#}\mu_0$, the pushforward formula, the straight-line identity, and $F_{\Phi} = T_p$ $\mu_0$-almost everywhere give

$$\begin{aligned}\frac{1}{p} \int_0^1 \int_{\mathbb{R}^d} \|v_{\Phi}(t,y)\|^p \, \rho_t^{\Phi}(\mathrm{d}y)\, \mathrm{d}t &= \frac{1}{p} \int_0^1 \int_{\mathbb{R}^d} \big\|v_{\Phi}\big(t, z_{\Phi}(t,x)\big)\big\|^p \, \mu_0(\mathrm{d}x)\, \mathrm{d}t \\ &= \frac{1}{p} \int_0^1 \int_{\mathbb{R}^d} \|T_p(x) - x\|^p \, \mu_0(\mathrm{d}x)\, \mathrm{d}t \\ &= \frac{1}{p} \int_{\mathbb{R}^d} \|T_p(x) - x\|^p \, \mu_0(\mathrm{d}x) \\ &= \frac{1}{p} W_p^p(\mu_0, \mu_1).\end{aligned}$$

The generalized Benamou–Brenier formula states that $W_p^p(\mu_0, \mu_1)/p$ is the minimum of the dynamic action. Since each absolutely continuous trajectory $z_{\Phi}(\cdot, x)$ satisfies the characteristic equation almost everywhere in time and $\rho_t^{\Phi} = (z_{\Phi}(t, \cdot))_{\#}\mu_0$, the standard characteristic-flow argument implies that $(\rho_t^{\Phi}, v_{\Phi})$ satisfies the continuity equation in the distributional sense. Together with the

endpoint conditions $\rho_0^\Phi = \mu_0$ and $\rho_1^\Phi = \mu_1$, the preceding action identity therefore shows that $(\rho_t^\Phi, v_\Phi)$ is a minimizer of the $p$-Benamou–Brenier problem.

Finally, for $\mu_0$-almost every $x$,

$$z_\Phi(t,x) = (1-t)x + tT_p(x) \qquad \text{for every } t \in [0,1],$$

and

$$v_\Phi\big(t, z_\Phi(t,x)\big) = T_p(x) - x \qquad \text{for every } t \in (0,1).$$

The Benamou–Brenier solution $(\rho^\star, v^\star)$ from part (1) is induced by the same optimal map $T_p$, and both velocity fields equal $T_p(x) - x$ along the common trajectory $(1-t)x + tT_p(x)$, $\mathrm{d}t \otimes \mu_0$-almost everywhere. Since

$$\rho_t^\Phi = \big((1-t)\,\mathrm{Id} + tT_p\big)_\sharp \mu_0 = \rho_t^\star,$$

the pushforward formula gives

$$\begin{aligned}
&\int_0^1 \int_{\mathbb{R}^d} \|v_\Phi(t,y) - v^\star(t,y)\|^p \; \rho_t^\Phi(\mathrm{d}y)\,\mathrm{d}t \\
=&\int_0^1 \int_{\mathbb{R}^d} \big\|v_\Phi\big(t,(1-t)x + tT_p(x)\big) - v^\star\big(t,(1-t)x + tT_p(x)\big)\big\|^p \; \mu_0(\mathrm{d}x)\,\mathrm{d}t \\
=&0.
\end{aligned}$$

Since the integrand on the left-hand side is nonnegative, it follows that

$$v_\Phi = v^\star \qquad \mathrm{d}t\,\rho_t^\Phi(\mathrm{d}y)\text{-almost everywhere.}$$

This proves both exact recovery and velocity-field uniqueness. □

### A.2 The Role and Non-Redundancy of Interior Full Support

Theorem 3.2 shows that a zero-loss potential $\Phi$ recovers the optimal transport map provided that $\Phi$ is $C^2$ on $(0,1) \times \mathbb{R}^d$ and the induced distribution $\rho_t^\Phi$ has full support for every $t \in (0,1)$. The interior $C^2$ regularity ensures that the differential calculations and chain-rule arguments in the proof are valid. A natural question is whether the full-support condition can be removed or replaced by a weaker assumption. The following counterexamples address this question. Counterexample 1 gives a zero-loss potential for which $\rho_t^\Phi$ does not have full support and the induced terminal map is not optimal; in this example, the target measure $\mu_1$ also fails to have full support. Counterexample 2 further shows that requiring $\mu_1$ itself to have full support is still insufficient to guarantee optimality.

Both counterexamples use $p = 2$. In this case $v_\Phi = -\nabla_x \Phi$, and hence, with $S_t(x) = (1-t)x + tF_\Phi(x)$,

$$\nabla_x \Phi\big(t, S_t(x)\big) + F_\Phi(x) - x = -\left[v_\Phi\big(t, S_t(x)\big) - \big(F_\Phi(x) - x\big)\right].$$

Thus the potential-matching residual is the negative of the velocity residual used in the former flow-matching formulation. Their squared norms are identical, so the two zero-loss conditions coincide in these examples.

**Counterexample 1: failure after removing interior full support.** Let $d = 2$, $p = 2$, and $c_2(x,y) = \|x-y\|^2/2$. Fix $M > \sqrt{8}$ and define

$$\begin{aligned}
a_- &:= (-2, -M/2), \quad u_- := (1, M), \qquad b_- := a_- + u_- = (-1, M/2), \\
a_+ &:= (2, M/2), \qquad u_+ := (-1, -M), \quad b_+ := a_+ + u_+ = (1, -M/2).
\end{aligned}$$

Choose $0 < r < 1/4$ and set

$$A_- := B(a_-, r/2), \qquad A_+ := B(a_+, r/2).$$

Define

$$\mu_0 := \frac{1}{2}\,\mathrm{Unif}(A_-) + \frac{1}{2}\,\mathrm{Unif}(A_+).$$

Define $F$ $\mu_0$-almost everywhere by

$$F(x) := \begin{cases} x + u_-, & x \in A_-, \\ x + u_+, & x \in A_+. \end{cases}$$

Define

$$\mu_1 := F_\sharp \mu_0.$$

Then

$$\operatorname{supp}(\mu_1) = \overline{B(b_-, r/2)} \cup \overline{B(b_+, r/2)} \neq \mathbb{R}^2.$$

We next construct a smooth potential whose flow agrees with $F$ on the support of $\mu_0$. Define the moving centers

$$c_-(t) := a_- + tu_-, \qquad c_+(t) := a_+ + tu_+, \qquad t \in [0,1].$$

Their first coordinates satisfy

$$\big(c_+(t)\big)_1 - \big(c_-(t)\big)_1 = 4 - 2t \geq 2.$$

Let $\chi \in C_c^\infty(\mathbb{R}^2)$ satisfy

$$\chi(\xi) = 1 \quad \text{for } \|\xi\| \leq r, \qquad \operatorname{supp}(\chi) \subset B(0, 2r).$$

Because $r < 1/4$, the two moving cutoff supports remain disjoint for all $t \in [0,1]$. Define

$$\begin{aligned} \Phi(t,y) := & -\chi\big(y - c_-(t)\big) u_- \cdot \big(y - c_-(t)\big) \\ & -\chi\big(y - c_+(t)\big) u_+ \cdot \big(y - c_+(t)\big), \end{aligned}$$

and let $v_\Phi = -\nabla_y \Phi$. On $B(c_-(t), r)$, the first cutoff is identically one and the second vanishes, so

$$v_\Phi(t,y) = u_-.$$

Similarly, $v_\Phi(t,y) = u_+$ on $B(c_+(t), r)$. The potential $\Phi$ is smooth on $[0,1] \times \mathbb{R}^2$, and $v_\Phi$ is smooth with uniformly compact spatial support. Hence it generates a unique global smooth flow, and every time slice $z_\Phi(t,\cdot)$ is a diffeomorphism of $\mathbb{R}^2$.

For $x \in A_-$, the curve $z(t) = x + tu_-$ satisfies

$$\|z(t) - c_-(t)\| = \|x - a_-\| < r/2 < r,$$

and therefore

$$\partial_t z(t) = u_- = v_\Phi\big(t, z(t)\big).$$

Uniqueness of the flow gives $z_\Phi(t,x) = x + tu_-$ for every $t \in [0,1]$. The same argument gives $z_\Phi(t,x) = x + tu_+$ for $x \in A_+$. Consequently, for $\mu_0$-almost every $x$,

$$z_\Phi(t,x) = (1-t)x + tF(x), \qquad F_\Phi(x) = z_\Phi(1,x) = F(x).$$

It follows that

$$v_\Phi\big(t, (1-t)x + tF_\Phi(x)\big) = F_\Phi(x) - x$$

for every $t \in [0,1]$ and for $\mu_0$-almost every $x$. Thus $\mathcal{L}_{\mathrm{PM}}(\Phi) = 0$. Since $(F_\Phi)_\sharp \mu_0 = \mu_1$, the terminal loss also vanishes, and hence

$$\mathcal{L}_{\mathrm{PMOT}}(\Phi) = 0.$$

Because the PMOT objective is nonnegative, $\Phi$ is a global minimizer. Nevertheless, its intermediate distributions occupy only two moving tubes:

$$\operatorname{supp}(\rho_t^\Phi) = \overline{B(c_-(t), r/2)} \cup \overline{B(c_+(t), r/2)} \neq \mathbb{R}^2, \qquad t \in [0,1].$$

The induced coupling is not optimal. Since the density of $\mu_0$ is strictly positive near $a_-$ and $a_+$ and $F$ is a translation on each ball, both $(a_-, b_-)$ and $(a_+, b_+)$ belong to the support of

$$\pi := (\mathrm{Id}, F)_\sharp \mu_0.$$

The cost of the assigned pairing is

$$c_2(a_-, b_-) + c_2(a_+, b_+) = \frac{1}{2}\|u_-\|^2 + \frac{1}{2}\|u_+\|^2 = 1 + M^2.$$

After exchanging the endpoints, $a_- - b_+ = (-3, 0)$ and $a_+ - b_- = (3, 0)$, so

$$c_2(a_-, b_+) + c_2(a_+, b_-) = 9.$$

Since $M > \sqrt{8}$, we have $1 + M^2 > 9$. Thus the support of $\pi$ violates the two-point $c_2$-cyclical-monotonicity inequality, and $\pi$ is not an optimal coupling between $\mu_0$ and $\mu_1$.

Thus, without interior full support, a smooth potential may attain zero PMOT loss while inducing a nonoptimal terminal map. The obstruction is the persistent vacuum outside the two moving tubes: the potential-matching loss constrains the potential gradient, and equivalently the velocity in the quadratic case, only along mass-carrying trajectories, so the material-derivative identity cannot be extended to the entire interior space–time domain.

**Counterexample 2: terminal full support does not replace interior full support.** In Counterexample 1, the target measure $\mu_1$ does not have full support. The following example further shows that even the condition $\mathrm{supp}(\mu_1) = \mathbb{R}^d$ is insufficient to guarantee that a zero-loss terminal map is optimal when the intermediate distributions fail to have full support.

Let $d = 2$, $p = 2$, and fix $M > \sqrt{8}$. Define

$$K_- := \{x \in \mathbb{R}^2 : x_1 < -1\}, \qquad K_+ := \{x \in \mathbb{R}^2 : x_1 > 1\},$$

and set

$$a_- := (-2, -M/2), \qquad a_+ := (2, M/2).$$

For suitable normalizing constants $Z_-, Z_+ > 0$, let

$$f_-(x) := \frac{1}{Z_-} e^{-\|x-a_-\|^2} \mathbf{1}_{K_-}(x), \qquad f_+(x) := \frac{1}{Z_+} e^{-\|x-a_+\|^2} \mathbf{1}_{K_+}(x),$$

and define

$$\mu_0(\mathrm{d}x) := \frac{1}{2} f_-(x)\,\mathrm{d}x + \frac{1}{2} f_+(x)\,\mathrm{d}x.$$

Then $\mu_0 \ll \mathcal{L}^2$ and $\mu_0 \in \mathcal{P}_2(\mathbb{R}^2)$.

Let

$$u_- := (1, M), \qquad u_+ := (-1, -M),$$

and define

$$F(x) := \begin{cases} x + u_-, & x \in K_-, \\ x + u_+, & x \in K_+, \end{cases} \qquad \mu_1 := F_\sharp \mu_0.$$

Since $F(K_-) = \{y_1 < 0\}$ and $F(K_+) = \{y_1 > 0\}$, we have

$$\mathrm{supp}(\mu_1) = \mathbb{R}^2.$$

For $S_t(x) := (1-t)x + tF(x)$ and $\rho_t := (S_t)_\sharp \mu_0$,

$$\mathrm{supp}(\rho_t) = \{y_1 \le -(1-t)\} \cup \{y_1 \ge 1 - t\} \neq \mathbb{R}^2, \qquad t \in (0, 1).$$

Choose a smooth nondecreasing function $\vartheta \in C^\infty(\mathbb{R}; [0, 1])$ such that

$$\vartheta(r) = 0 \quad \text{for } r \le -1, \qquad \vartheta(r) = 1 \quad \text{for } r \ge 1,$$

and define, for $(t, y) \in (0, 1) \times \mathbb{R}^2$,

$$\Phi(t, y) := \left(2\vartheta\left(\frac{y_1}{1-t}\right) - 1\right)(y_1 + My_2).$$

The values of $\Phi$ at $t = 0$ and $t = 1$ may be chosen arbitrarily. Then $\Phi \in C^\infty((0, 1) \times \mathbb{R}^2)$. If $y_1 < -(1-t)$, then

$$\Phi(t, y) = -(y_1 + My_2), \qquad v_\Phi(t, y) = -\nabla_y \Phi(t, y) = (1, M) = u_-.$$

Similarly, if $y_1 > 1 - t$, then

$$\Phi(t, y) = y_1 + My_2, \qquad v_\Phi(t, y) = (-1, -M) = u_+.$$

For every $x \in K_- \cup K_+$ and $t \in (0,1)$, the straight-line trajectory $S_t(x)$ remains in the corresponding occupied component. Hence

$$v_\Phi\big(t, S_t(x)\big) = F(x) - x = \partial_t S_t(x).$$

Thus $F_\Phi = F$ $\mu_0$-almost everywhere, and

$$\mathcal{L}_{\mathrm{PM}}(\Phi) = 0, \qquad \mathcal{L}_{\mathrm{term}}(\Phi) = 0, \qquad \mathcal{L}_{\mathrm{PMOT}}(\Phi) = 0.$$

In particular, $\Phi \in \mathrm{dom}(\mathcal{L}_{\mathrm{PMOT}})$ and is a global minimizer.

Nevertheless, $F$ is not optimal. Let

$$x_- := a_-, \qquad x_+ := a_+, \qquad y_- := F(x_-) = (-1, M/2), \qquad y_+ := F(x_+) = (1, -M/2).$$

For $c_2(x,y) = \|x-y\|^2/2$,

$$\begin{aligned} c_2(x_-, y_-) + c_2(x_+, y_+) &= 1 + M^2, \\ c_2(x_-, y_+) + c_2(x_+, y_-) &= 9. \end{aligned}$$

Since $M > \sqrt{8}$, the first quantity is larger than the second. Moreover, the density of $\mu_0$ is positive near $x_-$ and $x_+$, so $(x_-, y_-)$ and $(x_+, y_+)$ belong to the support of $(\mathrm{Id}, F)_\sharp \mu_0$. Hence this support is not $c_2$-cyclically monotone, and $(\mathrm{Id}, F)_\sharp \mu_0$ is not an optimal coupling.

Thus $\mathcal{L}_{\mathrm{PMOT}}(\Phi) = 0$ and $\mathrm{supp}(\mu_1) = \mathbb{R}^2$, but $F_\Phi$ is not an optimal Monge map. Terminal full support therefore does not replace the interior full-support condition in Theorem 3.2.

# B Additional Experimental Results

## B.1 Additional Toy Generation Results

Figure 5 shows unconditional generation results on the two-dimensional toy benchmarks. Samples are generated by transporting standard Gaussian samples through the learned inverse flow. These results verify endpoint generation quality, while the main text focuses on transport geometry and $p$-specific alignment.

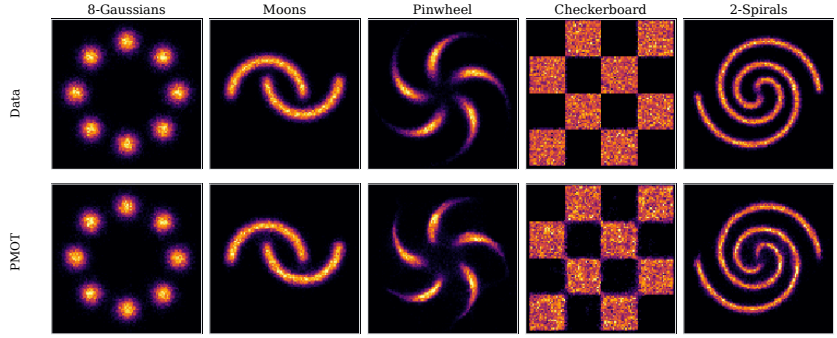



Figure 5: Unconditional generation on two-dimensional toy benchmarks. The top row shows samples from the target distributions, and the bottom row shows samples generated by PMOT from a standard Gaussian prior. All panels use the same two-dimensional histogram visualization protocol.

## B.2 Repeated $p$-Swap Evaluation on Pinwheel

In the main text, Figure 1 shows a representative $p$-swap evaluation on Pinwheel. To verify that the diagonal preference is not due to a particular evaluation sample, we repeat the evaluation over five independently sampled source and reference batches. For each repetition, we compute the mean endpoint MSE over the diagonal entries, corresponding to matched training and reference exponents, and over the off-diagonal entries, corresponding to mismatched exponents.

Table 4: Repeated $p$-swap evaluation on Pinwheel. Diagonal entries compare each PMOT checkpoint with the Sinkhorn barycentric reference computed using the matching exponent. Off-diagonal entries use mismatched reference exponents. Values are averaged over the corresponding heatmap entries in each evaluation repetition and reported as mean $\pm$ standard deviation.

| Evaluations | Diagonal MSE ↓ | Off-diagonal MSE ↓ | Off/Diagonal |
|---|---|---|---|
| 5 resamples | $0.0255 \pm 0.0031$ | $0.0359 \pm 0.0034$ | $1.410 \pm 0.048$ |

Table 5: Likelihood-weight sensitivity on POWER. PMOT weights are reported as $(\lambda_{\mathrm{PM}}, \lambda_{\mathrm{NLL}})$, while OT-Flow weights are reported as $(\lambda_L, \lambda_C, \lambda_R)$. OT-Flow keeps its kinetic and HJB/R coefficients fixed while varying $\lambda_C$. Evaluation uses biased MMD with 4000 generated and 4000 held-out samples. Lower is better.

| Method | Weights | NLL ↓ | MMD ↓ |
|---|---|---|---|
| PMOT | $(1, 5)$ | -0.383 | $2.91\times10^{-4}$ |
| OT-Flow | $(1, 10, 5)$ | -0.250 | $3.83\times10^{-4}$ |
| OT-Flow | $(1, 50, 5)$ | -0.287 | $3.91\times10^{-4}$ |
| OT-Flow | $(1, 500, 5)$ | -0.312 | $3.57\times10^{-4}$ |

Across the five evaluation repetitions, the mean off-diagonal endpoint MSE is $1.410 \pm 0.048$ times the mean diagonal MSE, corresponding to an average increase of $41.0\%$. This indicates that the fixed PMOT checkpoints are consistently closer to post-hoc OT references computed with their matching cost exponents. These repetitions measure evaluation-sample variability rather than variability across independent training runs.

### B.3 Likelihood-Weight Sensitivity on POWER

Table 5 reports an additional likelihood-weight sensitivity study on POWER. PMOT uses the same fixed weights $(\lambda_{\mathrm{PM}}, \lambda_{\mathrm{NLL}}) = (1, 5)$ as in the main high-dimensional experiments and does not include an HJB/R regularizer. For OT-Flow, we keep the kinetic and HJB/R coefficients fixed and vary only the likelihood coefficient $\lambda_C$.

Increasing the OT-Flow likelihood coefficient improves NLL on POWER, although generation MMD varies non-monotonically. PMOT achieves lower NLL and MMD with the fixed $(1, 5)$ weighting and no HJB/R regularizer. Together with the 8-Gaussians sensitivity experiment, these results suggest that PMOT remains effective without a heavily likelihood-dominated objective.

### B.4 High-Dimensional Training Configurations

Table 6 records the training configurations stored with the checkpoints used in Table 3. Both methods use two residual blocks ($n_{\mathrm{Th}} = 2$). The reported NLL values come from the validation-selected checkpoint of a single seed (0) for each configuration; the table documents the evaluated runs rather than asserting equal wall-clock or tuning budgets.

### B.5 High-Dimensional MMD Evaluation

We evaluate generated samples with a multiscale Gaussian-kernel MMD$^2$ (Gretton et al., 2012) in the standardized feature space used to train the tabular models. For each dataset, we first determine a single squared reference bandwidth $\sigma_d^2$ from the median pairwise squared distance on the training split. This bandwidth is fixed across methods and evaluation repetitions. The kernel is the equally weighted mixture

$$k_d(u, v) = \frac{1}{5} \sum_{c \in \{1/4, 1/2, 1, 2, 4\}} \exp\left( -\frac{\|u - v\|_2^2}{2c\sigma_d^2} \right). \tag{7}$$

Table 6: Checkpoint configurations for the high-dimensional experiments. Here $m$ is the hidden width and $n_t$ is the number of RK4 steps used during training.

| Dataset | Method | $m$ | $n_t$ | Iterations | Batch size | Learning rate |
|---|---|---|---|---|---|---|
| MiniBooNE | PMOT | 256 | 6 | 10,000 | 2,000 | 0.003 |
| | OT-Flow | 256 | 6 | 8,000 | 2,000 | 0.020 |
| POWER | PMOT | 128 | 10 | 36,000 | 4,096 | 0.003 |
| | OT-Flow | 128 | 10 | 36,000 | 10,000 | 0.030 |
| HEPMASS | PMOT | 256 | 12 | 40,000 | 2,000 | 0.003 |
| | OT-Flow | 256 | 12 | 40,000 | 2,000 | 0.020 |

Table 7: Multiscale unbiased $\mathrm{MMD}^2$ on high-dimensional tabular data. Values are $10^4 \times \mathrm{MMD}^2$ and are arithmetic means over 20 paired large-sample evaluations. The real-versus-real column compares two disjoint subsets of the held-out test split. Lower is better.

| Dataset | PMOT | OT-Flow | Real vs. real |
|---|---|---|---|
| MiniBooNE | 1.402 | 0.658 | -0.400 |
| POWER | 0.106 | 1.069 | 0.143 |
| HEPMASS | 0.343 | 0.093 | 0.015 |

The bandwidth calculation uses 5,000 training examples, draws up to 200,000 random index pairs, and excludes self-pairs before taking the median. It depends only on real training data and is not tuned separately for either model.

For generated samples $X = \{x_i\}_{i=1}^n$ and held-out test samples $Y = \{y_i\}_{i=1}^n$, we use the unbiased U-statistic

$$\widehat{\mathrm{MMD}}_u^2(X, Y) = \frac{1}{n(n-1)} \sum_{i \neq j} k_d(x_i, x_j) + \frac{1}{n(n-1)} \sum_{i \neq j} k_d(y_i, y_j) - \frac{2}{n^2} \sum_{i,j} k_d(x_i, y_j). \quad (8)$$

Each repetition draws $n = 3{,}600$ generated and held-out test samples for MiniBooNE and $n = 10{,}000$ for POWER and HEPMASS. Thus, each MiniBooNE evaluation uses all but 48 of its 3,648 test examples. PMOT and OT-Flow use the same 20 evaluation seeds and test subsets. We retain negative finite-sample estimates rather than clipping them, and report their arithmetic mean. The real-versus-real reference is computed separately from two disjoint subsets of the same held-out test split, using 1,800 points per subset for MiniBooNE and 10,000 per subset for the other two datasets. These repetitions quantify evaluation-sampling variability, not variation across independent training runs. The inverse flows use 18 integration steps on MiniBooNE and 24 on POWER and HEPMASS, matching the numerical settings used for the corresponding NLL evaluation.

The method ordering is not consistent across datasets: OT-Flow has a lower mean on MiniBooNE and HEPMASS, whereas PMOT has a lower mean on POWER. Small negative real-versus-real entries are possible because the unbiased finite-sample estimator is not constrained to be nonnegative. A paired bootstrap over the 20 evaluation records preserves this ordering on each dataset; this stability analysis concerns evaluation sampling for fixed checkpoints rather than variation across retraining runs.

### B.6 Image Color Transformation

We use image color transformation to illustrate PMOT with sample-based terminal matching in RGB space. In this experiment, the terminal discrepancy in equation 5 is instantiated as MMD rather than the NLL objective used for toy and tabular density estimation. The learned forward flow transports the empirical color distribution of a content image toward that of a style image. The resulting map is applied independently to each pixel, so the spatial layout of the content image is retained.

We select two $256 \times 256$ images from ImageNet (Deng et al., 2009; Russakovsky et al., 2015): an American chameleon (synset n01682714) as the content image and a sulphur-crested cockatoo

Table 8: Final PMOT training losses for image color transformation.

| Method | $\mathcal{L}_{\mathrm{PM}}$ | $\mathcal{L}_{\mathrm{MMD}}$ |
|---|---|---|
| PMOT | $2.891 \times 10^{-3}$ | $6.664 \times 10^{-4}$ |

(synset n01819313) as the style image. Their empirical RGB distributions are treated as the source and target distributions, respectively. RGB values are rescaled to $(0, 1)^3$ and mapped to $\mathbb{R}^3$ using a componentwise logit transform. We train PMOT with $p = 2$, $(\lambda_{\mathrm{PM}}, \lambda_{\mathrm{MMD}}) = (1, 10)$, and a mixture of five Gaussian kernels with bandwidths $\sigma \in \{0.25, 0.5, 1.0, 2.0, 4.0\}$ for 25,000 iterations.

Table 8 reports the final training losses. Figure 4 visualizes the transformed image along the learned flow. The marginal RGB distributions in Figure 6 provide an additional qualitative comparison between the source, transformed, and target color distributions.

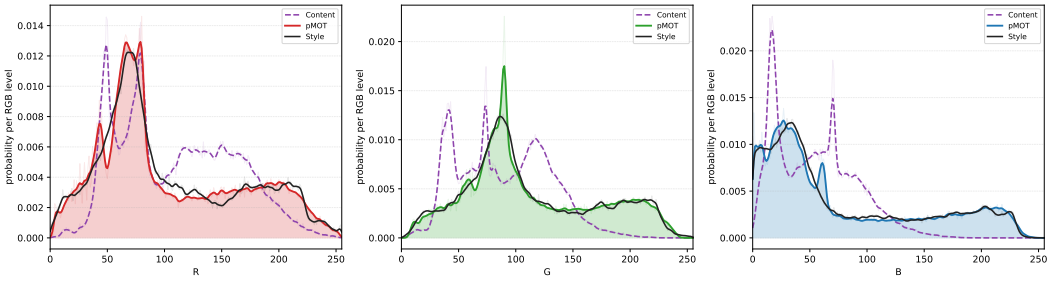



Figure 6: Marginal red, green, and blue distributions of the content image, the PMOT-transformed image, and the target style image. The transformed marginals move toward those of the target, providing qualitative evidence of color-distribution matching.